Electrochemical Evaluation of Self-Supported NiFe-LDH Electrocatalysts for Alkaline Urea Oxidation

Author Sultan Sarhan Alhayyani ssalhayyani@gmail.com

Mentor Prof. Guanjie He g.he@ucl.ac.uk

KAUST Academy Energy Specialization Summer Internship Program

Hosted by University College London (UCL), Department of Chemistry

Abstract

Self-supported anodic electrodes were assessed for alkaline urea oxidation using bare nickel foam (NF), a nominal NiFe-layered double hydroxide coating grown on nickel foam (NiFe-LDH/NF), and the corresponding coating grown on iron mesh (NiFe-LDH/Fe mesh). Measurements were conducted at room temperature in 1 M KOH and in 1 M KOH + 0.33 M urea using cyclic voltammetry (CV), forward-scan linear sweep voltammetry (LSV), and electrochemical impedance spectroscopy (EIS); morphology was examined by scanning electron microscopy (SEM). LSV potentials were converted to the reversible hydrogen electrode scale and corrected for 90% of the fitted series resistance. Among the complete electrode configurations tested, NiFe-LDH/NF required the lowest potentials at 50 and 100 mA cm^{-2}: 1.471 and 1.499 V in KOH, and 1.403 and 1.409 V in urea-containing electrolyte. Urea therefore lowered the matched-current potential of this electrode by 68 and 90 mV, respectively; a 156 mV reduction was measured at 500 mA cm^{-2} within the acquired scan range. These shifts are consistent with a strong urea-oxidation contribution at relatively low anodic potentials. Oxygen evolution nevertheless remains a competing reaction, especially at higher polarization, and electrochemical current alone cannot establish product selectivity. Local apparent Tafel slopes, EIS fits, and 50-cycle CV conditioning were used as comparative not mechanistically definitive descriptors. A 23.539 h chronopotentiometry record for NiFe-LDH/NF at 100 mA cm^{-2} showed an 88.59 mV increase between the 0.5–1.0 h and final 0.5 h mean potentials, with a record-wide linear drift of 5.00 mV h^{-1} after 300 s. Overall, NiFe-LDH/NF was the most promising tested configuration for urea-assisted electrolysis, while replicate electrodes, product analysis, phase/composition verification, and full-cell energy measurements remain necessary to demonstrate selectivity, treatment efficacy, and practical energy savings.

Date 20 August 2026

Contents

List of Figures ii

List of Tables iii

Abbreviations and Reporting Conventions iv

1 Introduction 1

1.1 Why replace oxygen evolution at the anode? . . . 1
1.2 Nickel redox mediation and the competing OER . . . 1
1.3 Why self-supported NiFe-type electrodes? . . . 2
1.4 Scope and questions addressed . . . 2

2 Experimental and Analytical Methods 3

2.1 Electrode matrix and comparison logic . . . 3
2.2 Substrate pretreatment and seed-assisted growth . . . 3
2.3 Scanning electron microscopy . . . 5
2.4 Electrochemical cell and measurement sequence . . . 5
2.5 Potential conversion, resistance correction, and benchmark extraction . . . 5
2.6 Apparent Tafel, CV, EIS, and stability analysis . . . 6

3 Results and Discussion 6

3.1 Morphology of the self-supported coatings . . . 6
3.2 Forward polarization: activity at matched current density . . . 8
3.3 Local apparent Tafel behaviour . . . 10
3.4 Impedance response and equivalent-circuit limits . . . 11
3.5 CV conditioning over 50 cycles . . . 12
3.6 Constant-current operational stability of NiFe-LDH/NF . . . 14
3.7 Integrated electrode assessment . . . 15

4 Study limitations and Recommended Future Work 17

4.1 Electrode comparison and reproducibility . . . 17
4.2 Reaction products and full-cell performance . . . 17
4.3 Material characterization . . . 17
4.4 Electrochemical analysis and durability . . . 18

5 Conclusions 19

Acknowledgements 19

References 20

List of Figures

1 Seed-assisted synthesis route for the self-supported electrodes. 4

2 Representative SEM morphology across substrate, coating, and aggregate length scales. Low-magnification images preserve the open-cell NF and woven Fe-mesh structures; intermediate and higher magnifications show micrometre-scale, flower-like aggregates assembled from sheet-like features. Instrument scale bars are retained. Intensity and contrast are not compared across acquisition sessions. . . . 7

3 Forward-scan polarization and matched-current comparison. (a,b) 90% iR-corrected LSVs at 5 mV s^{-1} in 1 M KOH and 1 M KOH + 0.33 M urea. (c) Potential reduction for NiFe-LDH/NF after adding urea at 50, 100, and 500 mA cm^{-2}; every value is interpolated within the measured current range. The 500 mA cm^{-2} comparison is available for this configuration but not for every electrode. 8

4 Local apparent Tafel fits. Markers show the selected experimental points and lines show ordinary least-squares fits to 90% iR-corrected potential. The slopes are comparative descriptors within narrow, manually selected windows and are not used to assign a unique rate-determining step. 10

5 Nyquist response at 0.650 V versus Ag/AgCl. Open symbols are measured data and lines are responses calculated from the saved ZView circuit parameters. The spectra were recorded at a common potential but different, frequently drifting DC currents. The Fe-mesh models contain no independently resolved R_{ct}. 11

6 Cyclic-voltammetry response at 50 mV s^{-1}. (a,b) Cycle-50 curves in KOH and KOH + urea. (c,d) Cycle 1 and cycle 50 for NiFe-LDH/NF. Potentials are converted to RHE and current is normalized to 1.00 cm^2 geometric area. Cycle-to-cycle changes indicate electrochemical evolution, not long-term durability. 13

7 Chronopotentiometric operation of NiFe-LDH/NF at 100 mA cm^{-2} in 1 M KOH + 0.33 M urea. (a) Raw 90% iR-corrected potential displayed every 10 s and a 30 min second-order Savitzky–Golay trend; the broad 1–3 V axis follows the requested presentation, while the inset exposes the actual drift. (b) Local derivative from the declared filter and project-specific ± 0.010 mV s^{-1} diagnostic bounds. No raw points were removed. The highlighted 16.4–17.2 h interval contains rapid fluctuations plausibly associated with bubble accumulation/release. 14

List of Tables

1 Terminology and conventions used throughout the report. iv
2 Electrode–electrolyte test matrix. "NiFe-LDH" is the operational sample name; phase and elemental composition were not independently verified in this work. . . 3
3 Audited forward-LSV benchmark potentials and maximum measured current density. 9
4 Audited local apparent Tafel fits. Current density is geometric and the fit windows contain only 5–6 points. 10
5 Q and n are CPE parameters. A dash under R_{ct} means the selected circuit did not contain that element, not that charge-transfer resistance was zero. 11
6 DC current recorded during each EIS spectrum. The broad drift, particularly for NF-based electrodes, limits strict equivalent-circuit interpretation. 12
7 Cycle-1/cycle-50 cathodic peak metrics and ascending-scan current ratio. $\Delta E_{pc} = E_{pc,50} - E_{pc,1}$. The current ratio is descriptive and is not a durability metric. 13
8 Operational-stability descriptors for NiFe-LDH/NF in urea-containing electrolyte. 15
9 Evidence-weighted comparison of the three tested complete electrode configurations. 16
10 Recommended experiments for extending and validating the findings of the present study. 18

Abbreviations and Reporting Conventions

Term	Meaning or convention
CV	Cyclic voltammetry.
EIS	Electrochemical impedance spectroscopy.
Fe mesh	Woven iron-mesh substrate; some source filenames use "Fe grid."
HER	Hydrogen evolution reaction at the cathode.
LDH	Layered double hydroxide; here an operational sample designation based on synthesis provenance.
LSV	Linear sweep voltammetry; forward scans are used for all primary comparisons.
NF	Nickel foam.
OER	Oxygen evolution reaction, a competing anodic reaction in urea-containing electrolyte.
RHE	Reversible hydrogen electrode potential scale.
UOR	Urea oxidation reaction.
E_x	90% iR-corrected potential required to reach x mA cm^{-2} in a forward LSV; no extrapolation is used.
j_{geo}	Current normalized to the projected geometric electrode area of 1.00 cm^2.
R_s; R_{ct}	Fitted series resistance; fitted charge-transfer resistance, respectively.

Table 1 Terminology and conventions used throughout the report.

Analysis convention

The title retains the project name "NiFe-LDH." In the body, this denotes a nominal NiFe-LDH-type coating prepared by the supplied seed-assisted protocol. SEM confirms morphology and coverage at selected locations but does not independently verify phase, composition, oxidation state, interlayer species, or catalyst loading.

1 Introduction

1.1 Why replace oxygen evolution at the anode?

Alkaline water electrolysis couples hydrogen evolution at the cathode to oxygen evolution at the anode. The oxygen evolution reaction (OER) is thermodynamically and kinetically demanding, and its multistep proton-coupled electron-transfer chemistry commonly imposes a large fraction of the practical cell voltage. Replacing OER with the oxidation of an abundant waste-derived molecule can, in principle, reduce the anodic potential while creating a route to chemical remediation. Urea is attractive in this context because it is present in urine, agricultural effluents, and several industrial streams, and its ideal six-electron oxidation can be coupled to hydrogen evolution.

For the ideal nitrogen/carbonate pathway in strongly alkaline solution,

$$CO(NH_2)_2 + 8OH^- \rightarrow N_2 + CO_3^{2-} + 6H_2O + 6e^-, \tag{1}$$

whereas alkaline OER is

$$4OH^- \rightarrow O_2 + 2H_2O + 4e^-. \tag{2}$$

The often-cited ideal thermodynamic cell voltage for urea-assisted hydrogen production is approximately 0.37 V, compared with 1.23 V for overall water splitting under standard thermodynamic conditions [1]. This comparison defines a thermodynamic opportunity, not a guaranteed practical voltage. Urea oxidation is chemically complex, and nickel-based electrodes can produce cyanate, nitrite, nitrate, carbonate, nitrogen, and other products in potential- and catalyst-dependent proportions [2, 3]. Because products were not quantified in the present project, potentials are reported directly versus RHE at matched geometric current density. A formal "UOR overpotential" referenced to an assumed six-electron nitrogen pathway is deliberately avoided.

1.2 Nickel redox mediation and the competing OER

Nickel-containing alkaline electrodes commonly develop a $Ni(OH)_2/NiOOH$ redox couple. A widely used mechanistic description treats electro-generated NiOOH as an oxidizing mediator:

$$Ni(OH)_2 + OH^- \rightleftharpoons NiOOH + H_2O + e^-, \tag{3}$$

followed by chemical or electrochemical reaction with adsorbed urea and regeneration of a lower-valent nickel state [4, 5]. This EC′-type picture explains why urea-dependent anodic current often emerges near the nickel oxidation feature. It is not a universal elementary mechanism: reconstruction, surface coverage, hydroxide activity, mass transport, and potential can change the dominant sequence.

Urea-free 1 M KOH is an *electrolyte control* that establishes anodic behaviour in the absence of urea, where OER becomes dominant at sufficiently positive potentials. In 1 M KOH + 0.33 M urea, UOR and OER can occur concurrently. A lower potential or larger current after adding urea is evidence for a urea-dependent anodic contribution, but electrochemical current alone cannot partition charge between UOR, OER, nickel oxidation, and double-layer charging. Recent studies directly demonstrate the competition between urea and water oxidation on nickel-based sites [6]. Accordingly, this report uses the cautious inference that UOR is likely the predominant Faradaic contribution at relatively low anodic potentials in the urea-containing electrolyte, while OER becomes increasingly competitive as polarization rises.

1.3 Why self-supported NiFe-type electrodes?

Directly grown, self-supported catalyst layers can remove polymer binders and added conductive carbon, shorten electron-transport paths, and improve mechanical contact between catalyst and current collector [7]. Nickel foam additionally supplies a three-dimensional, conductive, nickel-containing framework; iron mesh offers a geometrically different woven support. Ni–Fe coupling is relevant because iron can alter nickel redox energetics and adsorption, and NiFe nanosheets have demonstrated high UOR activity [8, 9]. The same chemistry also produces highly active alkaline OER materials, however, so iron incorporation cannot be assumed to confer UOR selectivity [10, 11].

Porous supports complicate quantitative benchmarking. Projected area does not equal electrochemically active area; catalyst loading, wetting, pore accessibility, and substrate contribution may differ substantially even when all electrodes expose a nominal 1.00 cm^2 geometric footprint [12, 13]. In this study, bare nickel foam provides a direct coating control for NiFe-LDH/NF. No bare iron-mesh control was recorded. Consequently, NiFe-LDH/NF and NiFe-LDH/Fe mesh are compared as *complete electrode configurations*; differences cannot be assigned uniquely to the substrate, the coating, or their interaction.

1.4 Scope and questions addressed

The study combines SEM, CV, forward-scan LSV, EIS, and constant-current operation to answer four practical questions:

1. Does the nominal NiFe-LDH coating improve the response of nickel foam relative to bare NF under identical electrolyte conditions?
2. Which complete tested configuration bare NF, NiFe-LDH/NF, or NiFe-LDH/Fe mesh reaches common geometric current densities at the lowest corrected potential?
3. How does adding 0.33 M urea change the anodic response, apparent local Tafel behaviour, and fitted impedance parameters?
4. Does the best-performing configuration maintain an operationally controlled potential during an approximately 24 h test at 100 mA cm^{-2}?

Key finding

The most decision-relevant result is a matched-current comparison: for NiFe-LDH/NF, adding 0.33 M urea lowered the 90% iR-corrected potential by 68 mV at 50 mA cm^{-2} and 90 mV at 100 mA cm^{-2}. This is consistent with a strong UOR contribution, while remaining agnostic about product selectivity.

2 Experimental and Analytical Methods

2.1 Electrode matrix and comparison logic

Six electrode–electrolyte combinations were evaluated (Table 2). All electrochemical current densities are normalized to a projected exposed area of 1.00 cm^2. The coated electrodes are self-supported: no polymer binder or separate conductive additive was used. The principal causal contrast is bare NF versus NiFe-LDH/NF within the same electrolyte. Comparisons involving NiFe-LDH/Fe mesh are configuration-level because a bare Fe-mesh control was not available.

Code	Substrate / coating	Electrolyte	Role in analysis
NF_KOH	Bare nickel foam	1 M KOH	Urea-free control; direct comparator for coated NF
NiFe_NF_KOH	NiFe-LDH/NF	1 M KOH	Coated-NF response without urea
NiFe_FE_KOH	NiFe-LDH/Fe mesh	1 M KOH	Complete Fe-mesh configuration without urea
NF_Urea	Bare nickel foam	1 M KOH + 0.33 M urea	Urea-containing bare-NF control
NiFe_NF_Urea	NiFe-LDH/NF	1 M KOH + 0.33 M urea	Primary UOR configuration
NiFe_FE_Urea	NiFe-LDH/Fe mesh	1 M KOH + 0.33 M urea	Complete Fe-mesh configuration with urea

Table 2 Electrode–electrolyte test matrix. "NiFe-LDH" is the operational sample name; phase and elemental composition were not independently verified in this work.

2.2 Substrate pretreatment and seed-assisted growth

The supplied laboratory method records nickel-foam pieces of 1 cm × 3 cm. NF was ultrasonicated sequentially in acetone, 3 M HCl, and deionized water for 15 min in each liquid, then vacuum-dried at 60 °C. Solution A was prepared by dissolving 1.069 g $Ni(NO_3)_2{\cdot}6H_2O$ (approximately 3.68 mmol) in 18 mL 2-propanol. Solution B contained 0.14625 g $FeSO_4{\cdot}7H_2O$ (approximately 0.526 mmol) in 6 mL deionized water, corresponding to a nominal Ni:Fe precursor molar ratio of approximately 7:1.

Solution B was added dropwise to solution A and stirred at 500 rpm for 10 min. After 5 min of natural sedimentation, a pretreated substrate was immersed vertically in the growth medium for 24 h at 25 °C. The resulting electrode was rinsed repeatedly with deionized water and vacuum-dried at 60 °C for 12 h. Project sample records identify nominal NiFe-LDH-type coatings prepared on NF and Fe mesh using the seed-assisted route. The supplied written method explicitly documents the NF pretreatment sequence but not a separate Fe-mesh pretreatment record; no unrecorded Fe-mesh cleaning step is inferred here. The seed-adsorption and heterogeneous-nucleation sequence in Figure 1 is a proposed growth rationale adapted from the supplied seed-assisted method and related work [14], rather than a directly observed mechanism in these samples.

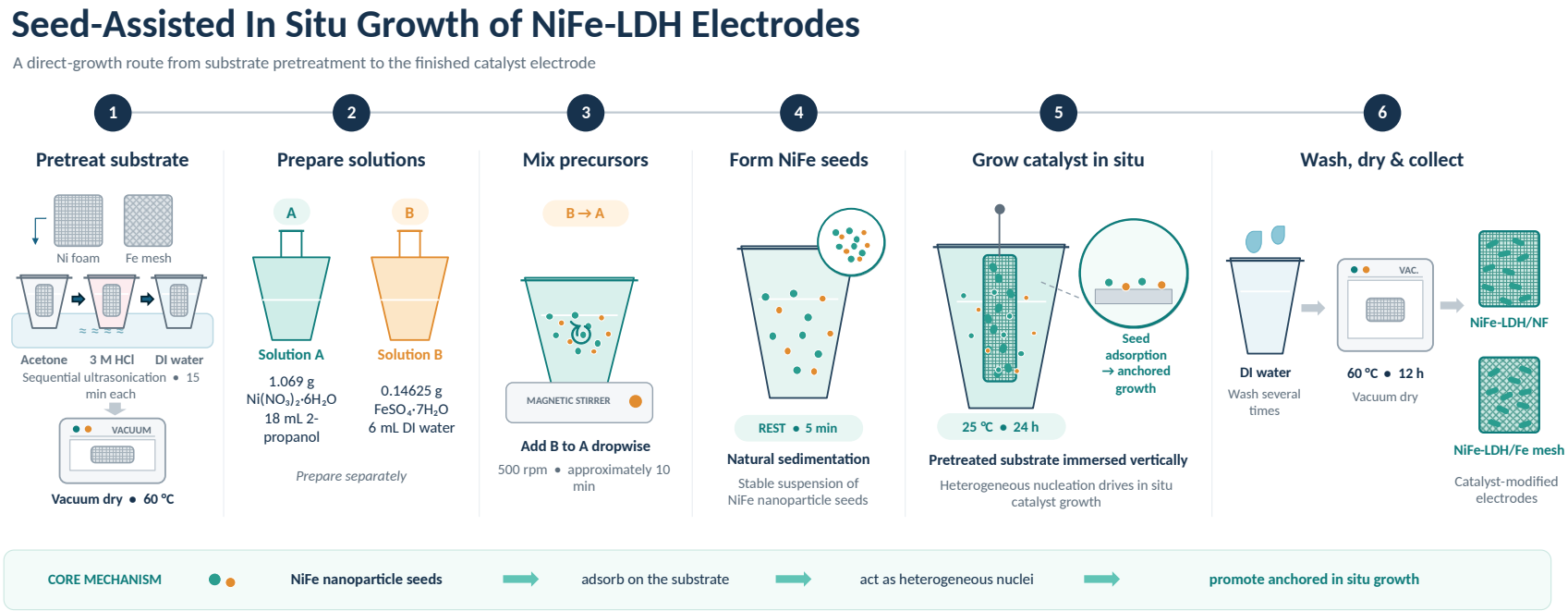


Figure 1 Schematic of the seed-assisted in situ growth protocol used to prepare binder-free NiFe-LDH/NF and NiFe-LDH/Fe-mesh electrodes. The seed-adsorption/heterogeneous-nucleation sequence is represented schematically. The source method explicitly records the NF cleaning sequence; Fe-mesh pretreatment details were not independently captured in the supplied method record.

2.3 Scanning electron microscopy

Representative surface fields were imaged by SEM at an accelerating voltage of 15.0 kV. The archived micrographs report working distances of 7.6–8.0 mm and include instrument scale bars. Images acquired at ×90, ×1900–2700, and ×5000–5500 were selected to compare substrate architecture, coating distribution, and aggregate morphology. SEM contrast was interpreted qualitatively; it was not used to derive coating thickness, composition, phase, loading, porosity, or electrochemically active surface area.

2.4 Electrochemical cell and measurement sequence

Measurements used a Gamry Interface 1010E potentiostat in a conventional three-electrode cell. The test electrode served as the working electrode, a saturated-KCl Ag/AgCl electrode as the reference, and a graphite rod as the counter electrode. The exposed geometric working-electrode area was 1.00 cm^2. Electrolytes were 1 M KOH and 1 M KOH + 0.33 M urea. Measurements are reported at room temperature; the unphysical temperature fields embedded in the raw instrument files were treated as metadata errors and were not used.

The measurement settings recovered from the raw files were:

- **CV:** 0.10–0.80 V versus Ag/AgCl (approximately 1.121–1.821 V versus RHE using the conversion below), 50 cycles, 50 mV s^{-1}, and a 5 mV potential step.
- **LSV:** 0.10–1.00 V versus Ag/AgCl, forward scan at 5 mV s^{-1} with a 5 mV step; instrument-level iR compensation was disabled.
- **EIS:** 0.650 V versus Ag/AgCl, 5 mV RMS perturbation, 100 kHz to 0.01 Hz, and 10 points per decade.
- **Chronopotentiometry:** 0.100 A applied to NiFe-LDH/NF in urea-containing electrolyte with 1 s sampling. The programmed duration was 48 h, but the recorded experiment terminated after 23.539 h and is flagged as aborted in the DTA file.

2.5 Potential conversion, resistance correction, and benchmark extraction

The existing analysis assumed pH 13.8 and used the saturated-KCl Ag/AgCl conversion

$$E_{\mathrm{RHE}} = E_{\mathrm{Ag/AgCl}} + 0.197 + 0.0597\,\mathrm{pH} = E_{\mathrm{Ag/AgCl}} + 1.02086\ \mathrm{V}. \tag{4}$$

The pH value is an analysis assumption rather than a value stored by the potentiostat; it therefore contributes a common systematic uncertainty. Forward LSV and chronopotentiometry potentials were corrected post hoc for 90% of the fitted series resistance:

$$E_{90\%\,iR} = E_{\mathrm{RHE}} - 0.90\,IR_{\mathrm{s}}, \tag{5}$$

where anodic current I is in amperes and R_{s} is the sample/electrolyte-specific ZView value. The raw curve was retained; no extrapolation was permitted. E_{10}, E_{50}, E_{100}, and E_{500} were obtained by linear interpolation between the adjacent measured points that bracketed the target current. A missing value means the current was not reached within the acquired scan.

Analysis convention

Because R_{s} was taken from nonstationary EIS spectra acquired at a common potential rather than a common current, the 90% iR correction should be read as a consistent comparative convention, not an uncertainty-free reconstruction of interfacial potential.

2.6 Apparent Tafel, CV, EIS, and stability analysis

Local apparent Tafel slopes were fitted as

$$E_{90\%\,iR} = a + b\log_{10}(j_{\mathrm{geo}}), \tag{6}$$

using manually selected 5–6-point windows around approximately 10 mA cm^{-2}. The windows span only 0.32–0.53 decades and no replicate uncertainty is available; b is therefore treated as a local descriptive slope, not a mechanism-diagnostic kinetic constant.

CV comparisons use the raw RHE-converted curves without post-iR correction. Cycle 50 is compared with cycle 1 through (i) the cathodic peak potential/current and (ii) the ascending-scan current ratio at 1.60 V. That ratio describes cycle-to-cycle evolution and is not labelled durability or current retention.

Three circuit forms were used by the saved analyses: $R_{\mathrm{s}} - (R_{\mathrm{ct}} \parallel \mathrm{CPE})$, $L - R_{\mathrm{s}} - (R_{\mathrm{ct}} \parallel \mathrm{CPE})$, and $L - R_{\mathrm{s}} - \mathrm{CPE}$. The latter contains no independently fitted R_{ct}. CPE coefficients are reported as model parameters and are not converted to capacitance. Only one saved fit contained a documented χ^2 value; missing fit statistics were not interpreted as zero.

For chronopotentiometry, Equation 5 used $R_{\mathrm{s}} = 0.98591\ \Omega$ from NiFe-LDH/NF in urea electrolyte. The raw 1 s trace was retained. A second-order, 1801-point (30 min) Savitzky–Golay filter was used only to display the slow trend and calculate a local derivative; no points were deleted from the quantitative record. The first comparison window was 0.5–1.0 h and the final window was the last 0.5 h. The ± 0.010 mV s^{-1} lines in the derivative plot are a project-specific diagnostic threshold supplied during data review, not a universal stability criterion.

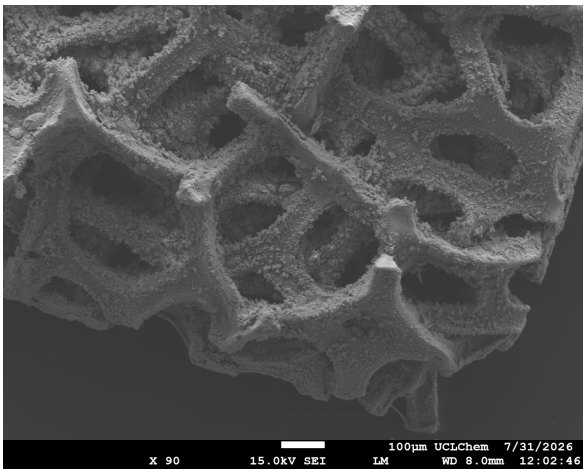
3 Results and Discussion

3.1 Morphology of the self-supported coatings

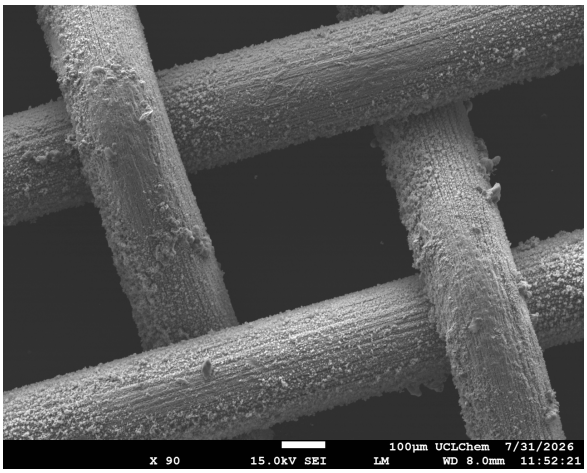
The low-magnification SEM images retain the defining architectures of the two supports (Figure 2a,b): an open-cell network for NF and a woven orthogonal-wire network for Fe mesh. This matters electrochemically because the support is not merely a planar current collector; it determines geometric roughness, local current distribution, gas-release pathways, and the area available for growth.

At intermediate magnification, both coated substrates show distributed micrometre-scale aggregates (Figure 2c,d). Higher-magnification fields resolve plate-like units assembled into open, flower-like structures (Figure 2e,f). The selected Fe-mesh field appears more spatially regular, whereas the selected NF field is more heterogeneous. Those visual impressions are qualitative: the images were acquired in different sessions and are not statistical maps of the full electrodes. Contrast and brightness cannot be compared quantitatively, and no conclusion about Ni:Fe ratio, crystallographic phase, coating thickness, mass loading, or active surface area follows from SEM alone.

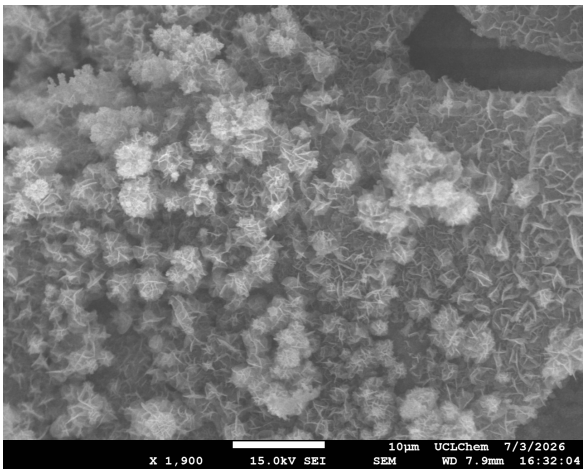
The open sheet-assembled morphology is plausibly favourable for electrolyte access and bubble disengagement, but this is a structure–function hypothesis rather than a measured transport property. Establishing such a relationship would require replicate imaging, loading measurements, and independent surface-area or capacitance analysis.



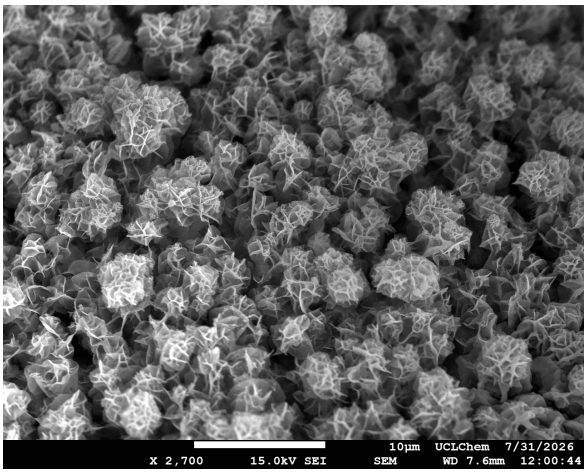
(a) NiFe-LDH/NF, ×90; 100 μm scale.



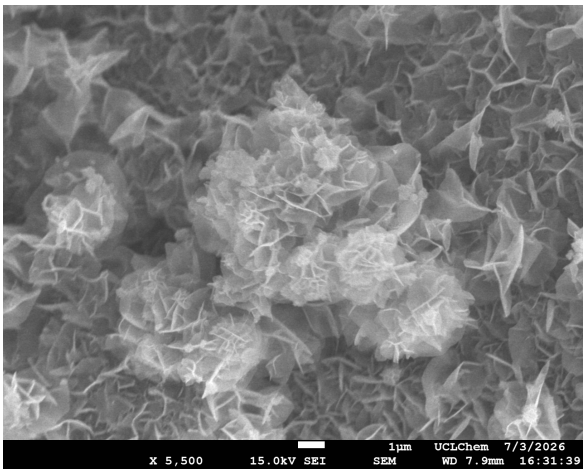
(b) NiFe-LDH/Fe mesh, ×90; 100 μm scale.



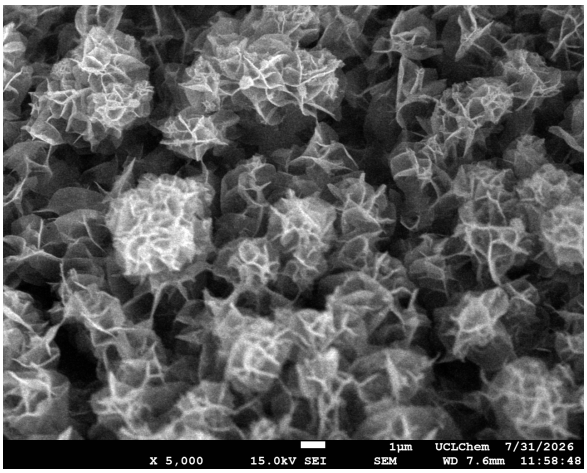
(c) NiFe-LDH/NF, ×1900; 10 μm scale.



(d) NiFe-LDH/Fe mesh, ×2700; 10 μm scale.



(e) NiFe-LDH/NF, ×5500; 1 μm scale.



(f) NiFe-LDH/Fe mesh, ×5000; 1 μm scale.

Figure 2 Representative SEM morphology across substrate, coating, and aggregate length scales. Low-magnification images preserve the open-cell NF and woven Fe-mesh structures; intermediate and higher magnifications show micrometre-scale, flower-like aggregates assembled from sheet-like features. Instrument scale bars are retained. Intensity and contrast are not compared across acquisition sessions.

3.2 Forward polarization: activity at matched current density

Figure 3a,b compares the 5 mV s^{-1} forward scans after the common RHE conversion and 90% iR correction. Table 3 reports interpolated potentials without extrapolation. The full curves contain nickel redox, catalyst reconstruction, Faradaic oxidation, capacitive current, and transport effects; E_x is therefore an operational polarization metric.

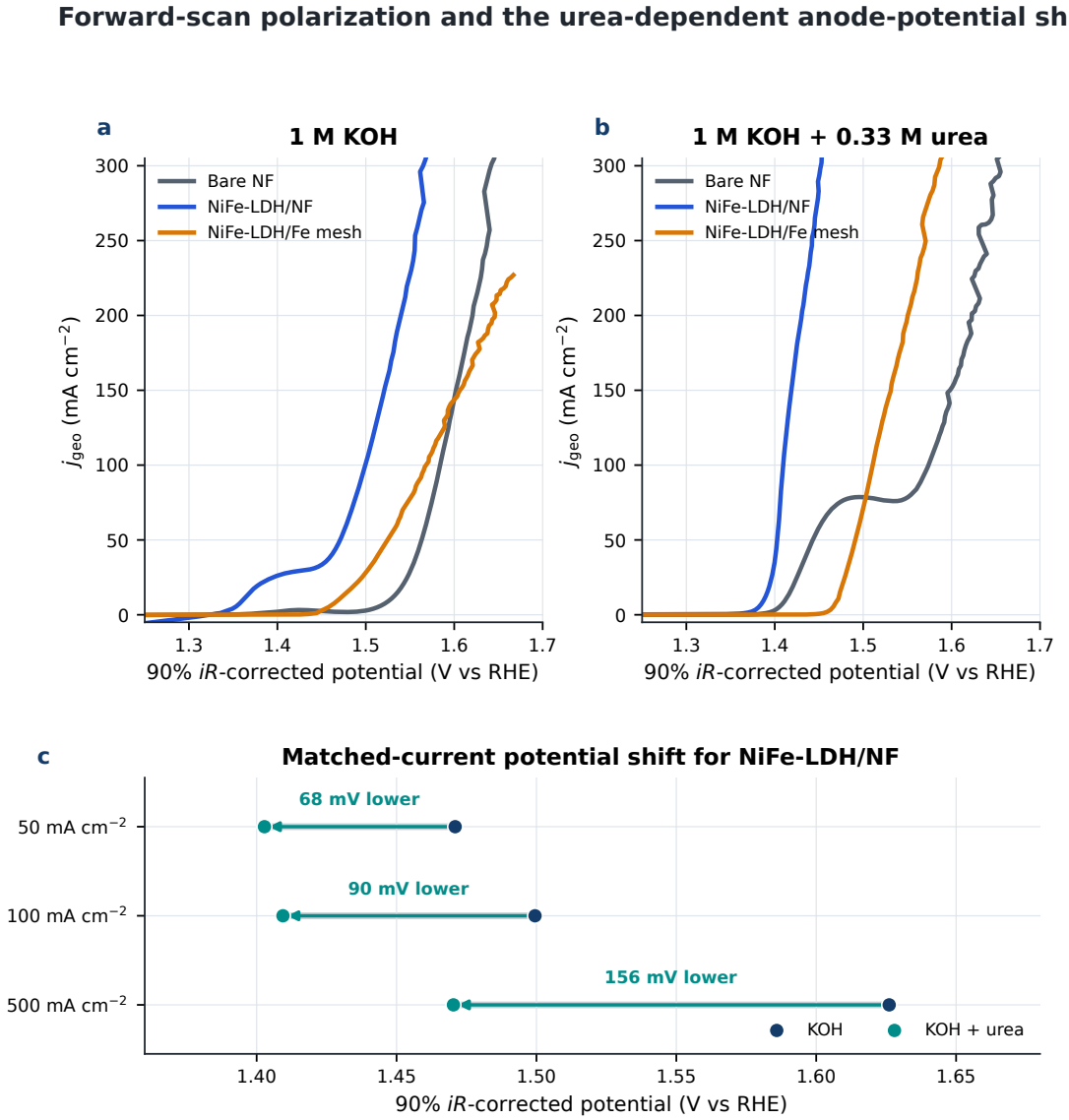


Figure 3 Forward-scan polarization and matched-current comparison. (a,b) 90% iR-corrected LSVs at 5 mV s^{-1} in 1 M KOH and 1 M KOH + 0.33 M urea. (c) Potential reduction for NiFe-LDH/NF after adding urea at 50, 100, and 500 mA cm^{-2}; every value is interpolated within the measured current range. The 500 mA cm^{-2} comparison is available for this configuration but not for every electrode.

Electrode	Electrolyte	E_{10}	E_{50}	E_{100}	E_{500}	j_{max}
		V vs RHE, 90% iR corrected				mA cm^{-2}
Bare NF	KOH	1.527	1.563	1.584	1.693	525
NiFe-LDH/NF	KOH	**1.361**	**1.471**	**1.499**	**1.626**	749
NiFe-LDH/Fe mesh	KOH	1.469	1.525	1.568	—	227
Bare NF	KOH + urea	1.412	1.443	1.574	—	324
NiFe-LDH/NF	KOH + urea	**1.388**	**1.403**	**1.409**	**1.470**	637
NiFe-LDH/Fe mesh	KOH + urea	1.471	1.491	1.511	—	472

Values are linearly interpolated between measured points. "—" means the target current was not reached; no extrapolation was performed. Bold identifies the lowest potential within each electrolyte at a given reached current.

Table 3 Audited forward-LSV benchmark potentials and maximum measured current density.

3.2.1 Effect of coating nickel foam

In urea-free KOH, coating NF lowered E_{50} by 92 mV and E_{100} by 85 mV relative to bare NF. At 500 mA cm^{-2}, both curves reached the target and the coated NF remained 67 mV lower. The exceptionally low E_{10} of 1.361 V for NiFe-LDH/NF occurs near the nickel oxidation feature. It should not be interpreted as an unambiguous steady-state OER potential because oxidation/reconstruction current can contribute strongly in this region [15]. The higher-current E_{50} and E_{100} comparisons are more decision-relevant.

In the urea electrolyte, NiFe-LDH/NF was 40 mV lower than bare NF at 50 mA cm^{-2} and 164 mV lower at 100 mA cm^{-2}. The sharp rise after the nickel redox region and the ability to reach 500 mA cm^{-2} at 1.470 V distinguish this electrode from the bare NF plateau and the more positive Fe-mesh response.

3.2.2 Effect of adding urea

The urea response was current-dependent. For NiFe-LDH/NF, urea increased E_{10} by 26.6 mV, but lowered E_{50}, E_{100}, and E_{500} by 68.2, 90.1, and 155.8 mV, respectively. The small adverse change at 10 mA cm^{-2} reinforces the nickel-redox caveat: the low-current KOH value is not a clean reaction-specific benchmark. For NiFe-LDH/Fe mesh, the urea shifts were +2.0, −33.6, and −57.5 mV at 10, 50, and 100 mA cm^{-2}. Bare NF showed large reductions at 10 and 50 mA cm^{-2} (−115 and −120 mV) but only 10 mV at 100 mA cm^{-2} because its urea curve passed through a broad current plateau.

These electrolyte-dependent shifts are consistent with a substantial UOR contribution. They do not prove that every measured electron came from UOR or that nitrogen was the oxidation product. At sufficiently positive potential, OER remains competitive, and the absence of O_2 detection or product/Faradaic-efficiency measurements prevents quantitative selectivity claims.

Key finding

NiFe-LDH/NF is the strongest configuration-level choice: it produced the lowest E_{50} and E_{100} in both electrolytes, and its urea-containing curve required 68 and 90 mV less potential than KOH at those matched currents. The result is robust as a polarization comparison, but not a product-selectivity measurement.

3.3 Local apparent Tafel behaviour

The audited local fits are shown in Figure 4 and quantified in Table 4. All R^2 values exceed 0.990 within the selected windows. This indicates local linearity; it does not establish that the region is free of nickel oxidation, bubble coverage, internal hydroxide gradients, or time-dependent reconstruction. Such non-kinetic effects can yield apparently excellent linear fits on porous NiFe electrodes [15, 16].

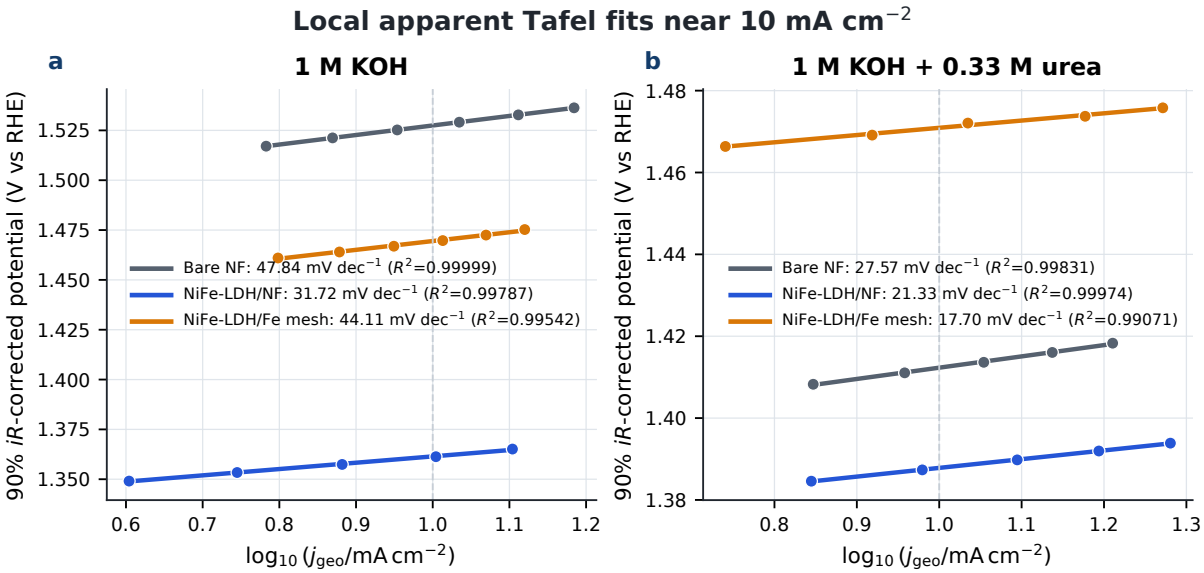


Figure 4 Local apparent Tafel fits. Markers show the selected experimental points and lines show ordinary least-squares fits to 90% iR-corrected potential. The slopes are comparative descriptors within narrow, manually selected windows and are not used to assign a unique rate-determining step.

Electrode	Electrolyte	Points	j range mA cm^{-2}	log$_{10}$ j span	b mV dec^{-1}	R^2
Bare NF	KOH	80–85 (6)	6.064–15.287	0.783–1.184	47.843	0.999990
NiFe-LDH/NF	KOH	46–50 (5)	4.018–12.705	0.604–1.104	31.722	0.997872
NiFe-LDH/Fe mesh	KOH	70–75 (6)	6.284–13.182	0.798–1.120	44.113	0.995415
Bare NF	KOH + urea	59–63 (5)	7.032–16.237	0.847–1.211	27.570	0.998313
NiFe-LDH/NF	KOH + urea	54–58 (5)	6.995–19.080	0.845–1.281	21.327	0.999738
NiFe-LDH/Fe mesh	KOH + urea	70–74 (5)	5.501–18.679	0.740–1.271	17.702	0.990709

Table 4 Audited local apparent Tafel fits. Current density is geometric and the fit windows contain only 5–6 points.

Adding urea reduced the local slope for each configuration: from 47.84 to 27.57 mV dec^{-1} for bare NF, 31.72 to 21.33 mV dec^{-1} for NiFe-LDH/NF, and 44.11 to 17.70 mV dec^{-1} for NiFe-LDH/Fe mesh. The smallest numerical slope therefore belongs to the Fe-mesh configuration in urea, although that electrode requires a substantially higher potential than NiFe-LDH/NF at 50 and 100 mA cm^{-2}. This internal inconsistency is informative: a local slope alone is not an activity ranking and does not directly prove faster charge transfer. NiFe-LDH/NF in KOH is also range-sensitive; broadening the window from the selected local points to roughly 5–20 mA cm^{-2} increases the fitted slope from 31.7 to approximately 42 mV dec^{-1} and degrades linearity. The values are

retained because they describe the acquired curves transparently, but mechanistic claims are withheld.

3.4 Impedance response and equivalent-circuit limits

All EIS spectra were acquired at the same nominal bias of 0.650 V versus Ag/AgCl (1.671 V versus RHE), not at a common current. Figure 5 overlays the measured Nyquist points and the responses calculated from the saved ZView circuit parameters. Low-frequency scatter and substantial within-spectrum current drift are visible. The fitted parameters are summarized in Table 5; the measured DC-current statistics are given in Table 6.

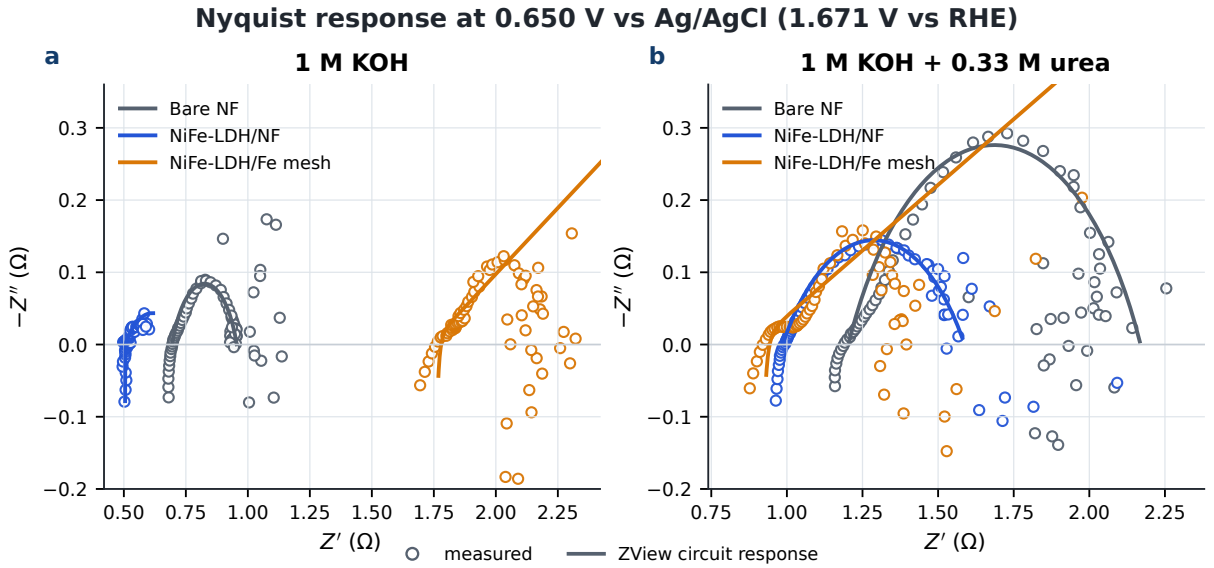


Figure 5 Nyquist response at 0.650 V versus Ag/AgCl. Open symbols are measured data and lines are responses calculated from the saved ZView circuit parameters. The spectra were recorded at a common potential but different, frequently drifting DC currents. The Fe-mesh models contain no independently resolved R_{ct}.

Electrode / electrolyte	Saved circuit	R_s (Ω)	R_{ct} (Ω)	Q ($\Omega^{-1}s^n$)	n	L (H)
Bare NF / KOH	$R_s - (R_{ct} \parallel \mathrm{CPE})$	0.69493	0.26022	0.030725	0.73206	—
NiFe-LDH/NF / KOH	$L - R_s - (R_{ct} \parallel \mathrm{CPE})$	0.50439	0.21855	1.571	0.48196	1.259×10^{-7}
NiFe-LDH/Fe mesh / KOH	$L - R_s - \mathrm{CPE}$	1.732	—	1.310	0.22316	9.029×10^{-8}
Bare NF / KOH + urea	$R_s - (R_{ct} \parallel \mathrm{CPE})$	1.203	0.96622	0.032721	0.66129	—
NiFe-LDH/NF / KOH + urea	$R_s - (R_{ct} \parallel \mathrm{CPE})$	0.98591	0.60149	0.15944	0.57021	—
NiFe-LDH/Fe mesh / KOH + urea	$L - R_s - \mathrm{CPE}$	0.89044	—	1.178	0.22175	9.081×10^{-8}

Table 5 Q and n are CPE parameters. A dash under R_{ct} means the selected circuit did not contain that element, not that charge-transfer resistance was zero.

Electrode	Electrolyte	Mean I_{dc} (A)	SD (A)	First → last (A)
Bare NF	KOH	0.109	0.011	0.133 → 0.084
NiFe-LDH/NF	KOH	0.247	0.084	0.305 → 0.117
NiFe-LDH/Fe mesh	KOH	0.0840	0.0007	0.0869 → 0.0824
Bare NF	KOH + urea	0.0800	0.0124	0.141 → 0.0585
NiFe-LDH/NF	KOH + urea	0.197	0.0098	0.231 → 0.180
NiFe-LDH/Fe mesh	KOH + urea	0.159	0.0058	0.171 → 0.145

Table 6 DC current recorded during each EIS spectrum. The broad drift, particularly for NF-based electrodes, limits strict equivalent-circuit interpretation.

Within the four spectra assigned a resolvable parallel R_{ct}, the coated NF had a smaller fitted value than bare NF in each electrolyte: 0.219 versus 0.260 Ω in KOH and 0.601 versus 0.966 Ω in KOH + urea. This is consistent with a lower fitted interfacial Faradaic impedance under those model and bias conditions. It is not proof of an intrinsically faster UOR, because the operating currents differ, the surface states evolve during acquisition, and OER can contribute at 1.671 V versus RHE. The Fe-mesh series-CPE models did not resolve an independent semicircle; comparing their nonexistent R_{ct} with the NF values would be invalid.

Only the NiFe-LDH/NF urea fit had a preserved χ^2 value (1.8924×10^{-4}); its CPE-Q uncertainty was 24.5%. Other parameter errors and residual statistics are missing rather than zero. Robust mechanistic EIS would require stationarity, residual inspection, uncertainty for every fit, and preferably Kramers–Kronig validation [17, 18].

3.5 CV conditioning over 50 cycles

Cycle-50 CVs and the evolution of NiFe-LDH/NF from cycle 1 to cycle 50 are shown in Figure 6. Quantitative descriptors appear in Table 7. The cathodic feature is attributed operationally to reduction of the oxidized nickel state; its location and magnitude evolve with wetting, reconstruction, surface coverage, and reaction with urea.

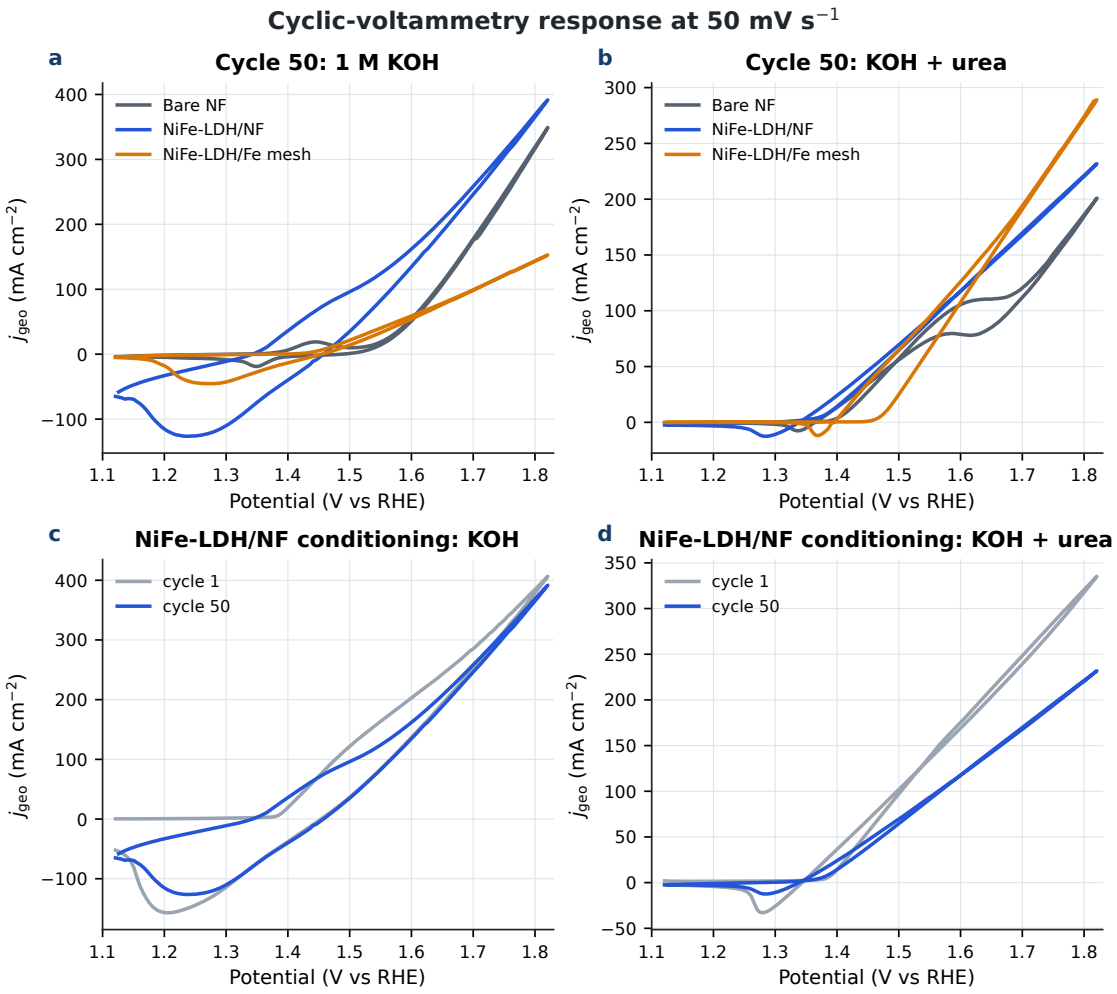


Figure 6 Cyclic-voltammetry response at 50 mV s^{-1}. (a,b) Cycle-50 curves in KOH and KOH + urea. (c,d) Cycle 1 and cycle 50 for NiFe-LDH/NF. Potentials are converted to RHE and current is normalized to 1.00 cm^2 geometric area. Cycle-to-cycle changes indicate electrochemical evolution, not long-term durability.

Electrode	Electrolyte	$E_{pc,1}$ (V)	$j_{pc,1}$ mA cm^{-2}	$E_{pc,50}$ (V)	$j_{pc,50}$ mA cm^{-2}	ΔE_{pc} (mV)	j_{50}/j_1 at 1.60 V (%)
Bare NF	KOH	1.35084	−9.350	1.35085	−18.838	+0.014	64.855
NiFe-LDH/NF	KOH	1.20593	−156.982	1.23587	−126.408	+29.934	79.767
NiFe-LDH/Fe mesh	KOH	1.30078	−34.189	1.27580	−45.426	−24.985	128.849
Bare NF	KOH + urea	1.33086	−4.358	1.33583	−7.631	+4.979	95.340
NiFe-LDH/NF	KOH + urea	1.28076	−32.993	1.28577	−12.480	+5.009	67.151
NiFe-LDH/Fe mesh	KOH + urea	1.36572	−15.894	1.37076	−11.787	+5.032	111.409

Table 7 Cycle-1/cycle-50 cathodic peak metrics and ascending-scan current ratio. $\Delta E_{pc} = E_{pc,50} - E_{pc,1}$. The current ratio is descriptive and is not a durability metric.

NiFe-LDH/NF in KOH exhibited the largest positive cathodic-peak shift (+29.9 mV) and a cycle-50/cycle-1 current ratio of 79.8% at 1.60 V. In urea, its cathodic peak shifted only +5.0 mV while the 1.60 V current ratio was 67.2%. Consumption of NiOOH by urea in an EC′-type process could contribute to changes in the reverse peak, consistent with nickel-mediated UOR [4, 5]; however, the data do not isolate that mechanism from reconstruction, passivation, catalyst loss, or altered wetting.

NiFe-LDH/Fe mesh showed ratios above 100% in both electrolytes (128.8% in KOH and 111.4% with urea), consistent with continuing activation or increasing accessible current during cycling. Bare NF in urea was closer to unity (95.3%). Even cycle 49 to cycle 50 changed by approximately −3.8% to +4.3% across the six tests, so universal conditioning completion cannot be claimed. The CV experiment is best viewed as a 50-cycle electrochemical-evolution test, not a substitute for long-duration stability or replicated before/after characterization.

3.6 Constant-current operational stability of NiFe-LDH/NF

NiFe-LDH/NF was selected for constant-current testing because it delivered the lowest matched-current potentials. The raw DTA record contains 84,742 points from 0 to 84,741 s, corresponding to 23.539 h, at a median current of 99.991 mA. Although the run was programmed for 48 h, it is explicitly flagged as aborted and is therefore reported only as an approximately 24 h experiment.

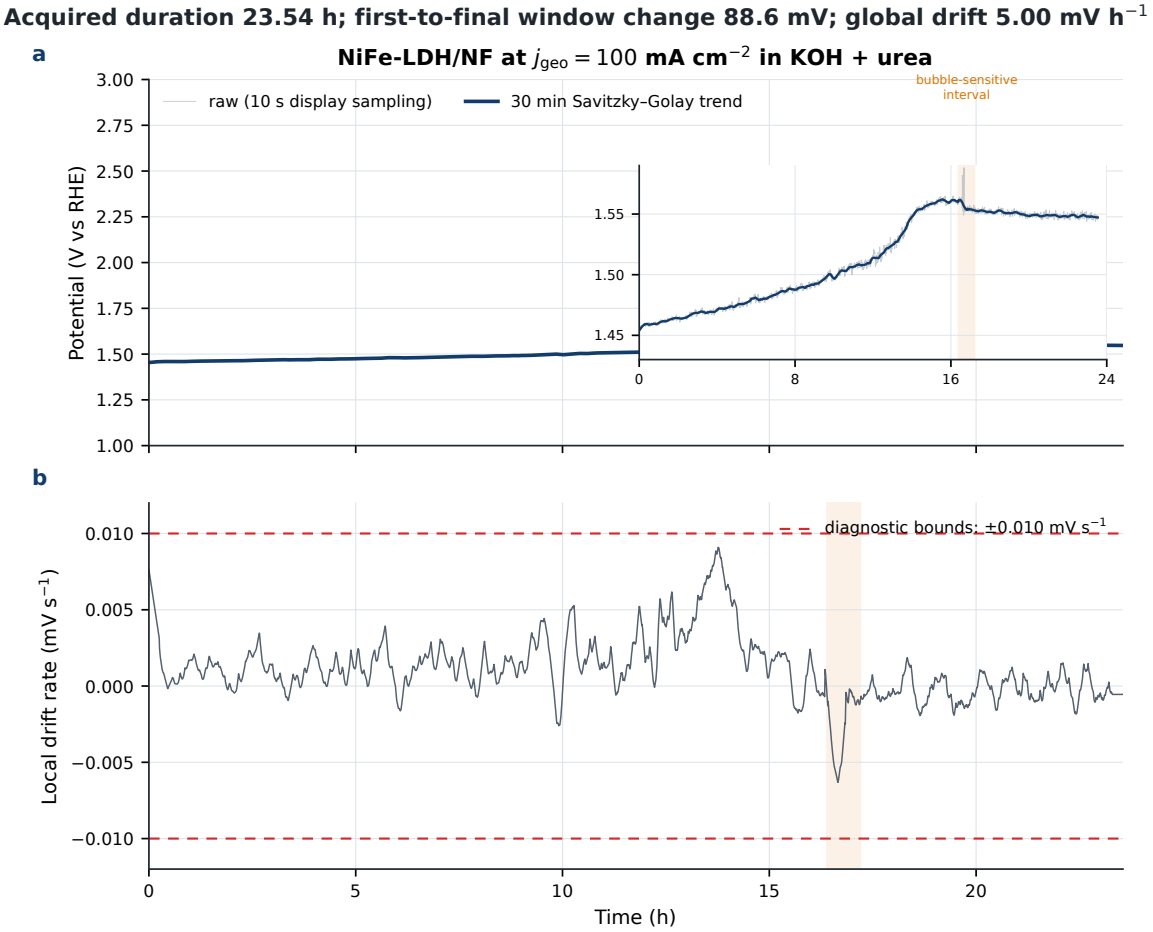


Figure 7 Chronopotentiometric operation of NiFe-LDH/NF at 100 mA cm^{-2} in 1 M KOH + 0.33 M urea. (a) Raw 90% *iR*-corrected potential displayed every 10 s and a 30 min second-order Savitzky–Golay trend; the broad 1–3 V axis follows the requested presentation, while the inset exposes the actual drift. (b) Local derivative from the declared filter and project-specific ±0.010 mV s^{-1} diagnostic bounds. No raw points were removed. The highlighted 16.4–17.2 h interval contains rapid fluctuations plausibly associated with bubble accumulation/release.

The mean corrected potential was 1.45910 V during 0.5–1.0 h and 1.54769 V during the final 0.5 h, an increase of 88.59 mV (approximately 6.07% of the initial-window value). A global least-squares slope after the first 300 s was +5.00 mV h^{-1}. The final-hour mean was 1.54799 $\pm$ 0.00171 V (mean $\pm$ standard deviation), indicating a comparatively narrow terminal fluctuation band after the preceding rise. This is not voltage constancy: the electrode required progressively more potential, particularly from approximately 13 to 16 h, before partial recovery and a plateau-like region.

The 30 min derivative ranged from -0.00632 to +0.00909 mV s^{-1}, inside the project-specific ± 0.010 mV s^{-1} threshold. Around 16.6–16.7 h, abrupt spike-and-drop behaviour is plausibly related to gas-bubble accumulation and release, which can perturb wetted area, solution resistance, and local current distribution [19]. That attribution is not extended to the broader 13–16 h rise, and the raw points are retained. Potential traces alone also cannot exclude urea depletion, carbonation, reference drift, surface reconstruction, or compensating changes in active area [20].

Chronopotentiometry descriptor	Audited value
Applied current / projected area	0.100 A / 1.00 cm^2
Actual recorded duration	23.539 h
Median current after 300 s	99.991 mA
Mean corrected potential, 0.5–1.0 h	1.45910 V vs RHE
Mean corrected potential, final 0.5 h	1.54769 V vs RHE
First-to-final window change	+88.59 mV
Global drift after 300 s	+5.00 mV h^{-1}
Final-hour potential	1.54799 $\pm$ 0.00171 V vs RHE
Local derivative range (30 min filter)	-0.00632 to +0.00909 mV s^{-1}

Table 8 Operational-stability descriptors for NiFe-LDH/NF in urea-containing electrolyte.

3.7 Integrated electrode assessment

Table 9 separates observations from interpretive strength. The most persuasive evidence is the raw-derived matched-current LSV ranking. Tafel and EIS provide supporting descriptors but are provisional because of narrow fit windows, nonstationarity, and heterogeneous circuits. CV documents ongoing surface evolution, and stability is available for only one electrode.

Criterion	Bare NF	NiFe-LDH/NF	NiFe-LDH/Fe mesh
Direct coating evidence	Baseline	Directly improves NF at 50/100 mA cm^{-2} in both electrolytes	Not isolable; no bare Fe-mesh control
Matched-current activity	Intermediate; urea plateau limits high-current response	Lowest E_{50} and E_{100} in both electrolytes; reaches 500 mA cm^{-2} in both	More positive than coated NF; does not reach 500 mA cm^{-2}
Urea-dependent shift	Large at 10/50 but only 10 mV at 100 mA cm^{-2}	68, 90, and 156 mV lower at 50, 100, and 500 mA cm^{-2}	34 and 57 mV lower at 50 and 100 mA cm^{-2}
Apparent Tafel descriptor	Moderate local slopes	Low local slopes with strongest activity	Lowest urea slope but poorer absolute activity; slope not an activity rank
EIS descriptor	Resolved R_{ct} under selected model	Lower fitted R_{ct} than bare NF within each electrolyte; nonstationary	No independently resolved R_{ct} in saved circuits
CV evolution	Condition-dependent; not fully stationary	Pronounced cycle evolution, especially KOH; current ratio below 100%	Ratios above 100%, consistent with continued activation
Overall decision	Essential control	**Most promising tested complete configuration**	Interesting secondary configuration; causal substrate claim unsupported

Table 9 Evidence-weighted comparison of the three tested complete electrode configurations.

The integrated interpretation is therefore deliberately narrow. NiFe-LDH/NF is the most promising electrode among those tested because it combines the lowest corrected matched-current potentials with a measurable high-current urea benefit and a dedicated constant-current record.

4 Study limitations and Recommended Future Work

The present study provides a consistent comparative evaluation of the tested electrode configurations under the same experimental framework. The results identify NiFe-LDH/NF as the most promising configuration among those examined and demonstrate that urea addition enables higher anodic current densities at lower potentials. The following considerations define the scope of these conclusions and highlight practical directions for extending the work.

4.1 Electrode comparison and reproducibility

Current densities were normalized to the same projected geometric area of 1.00 cm^2, allowing direct comparison of the complete electrode configurations under the applied conditions. However, catalyst loading and accessible surface area may differ between nickel foam and iron mesh because of their distinct structures and coating characteristics. In addition, the absence of a bare Fe-mesh control means that the individual contributions of the Fe-mesh substrate and the NiFe-LDH coating cannot yet be separated.

A useful extension would therefore compare bare NF, NiFe-LDH/NF, bare Fe mesh, and NiFe-LDH/Fe mesh using independently prepared replicate electrodes. Measuring catalyst loading would also allow geometric-current comparisons to be complemented by mass-normalized activity. These additions would strengthen the reproducibility of the observed trends and clarify how the substrate and catalyst coating each contribute to electrode performance.

4.2 Reaction products and full-cell performance

The polarization measurements show a clear urea-dependent anodic response, with lower potentials required after urea was introduced into the electrolyte. This supports the effectiveness of NiFe-LDH/NF for urea-assisted anodic oxidation under the conditions investigated. Product analysis would provide a valuable next step by determining the distribution of gaseous and dissolved products and quantifying the Faradaic efficiency of the reaction.

Suitable measurements could include gas analysis for O_2, N_2, and CO_2, together with analysis of dissolved nitrogen- and carbon-containing products and residual urea. Such measurements would clarify the dominant reaction pathways and distinguish UOR-derived current from competing OER contributions [2, 6].

The practical energy benefit of urea-assisted hydrogen production could subsequently be evaluated in a two-electrode cell. Comparing conventional water electrolysis and urea-assisted electrolysis under matched operating conditions would enable direct measurement of cell voltage, hydrogen production, urea conversion, product selectivity, and electrical-energy consumption.

4.3 Material characterization

SEM imaging confirms clear differences in surface morphology and supports the presence of a deposited coating on both substrates. Complementary characterization would provide further information about the chemical and structural properties of that coating. XRD or Raman spectroscopy could be used to support phase identification, while XPS and SEM–EDS could determine surface composition, oxidation states, and elemental distribution. Catalyst loading and possible metal leaching could also be assessed using ICP-based analysis.

Repeating selected characterization measurements after electrochemical operation would help relate changes in morphology or composition to the observed electrochemical behaviour and

long-term performance.

4.4 Electrochemical analysis and durability

The LSV, CV, Tafel, and EIS measurements collectively provide a useful assessment of polarization behaviour, apparent kinetics, and interfacial charge-transfer characteristics. Future studies could reinforce the kinetic analysis using quasi-steady-state current or potential steps and replicated measurements. EIS comparisons would also benefit from acquisition after a defined stabilization period and under matched operating conditions, supported by fitting residuals and consistency checks where appropriate [17, 18].

The 23.539 h constant-current experiment provides an informative initial assessment of operational behaviour. Longer replicated tests, for example over 48–100 h, would establish the reproducibility of the observed voltage evolution and allow more detailed evaluation of durability. Monitoring electrolyte conditions and performing pre- and post-test material characterization would further help distinguish reversible operational fluctuations, such as bubble accumulation and release, from persistent electrode changes.

Research objective	Recommended experiment	Expected contribution
Separate coating and substrate effects	Compare bare and NiFe-LDH-coated NF and Fe mesh using replicate electrodes	Clarify the contributions of catalyst coating and substrate architecture
Confirm reaction pathways	Analyse gaseous and dissolved products at selected potentials or currents	Determine product distribution and Faradaic efficiency
Strengthen material identification	Apply XRD/Raman, XPS, SEM–EDS, and loading analysis	Establish phase, composition, elemental distribution, and catalyst loading
Evaluate practical energy performance	Compare water and urea-assisted electrolysis in matched two-electrode cells	Quantify cell voltage, hydrogen production, urea conversion, and energy consumption
Assess long-term durability	Conduct replicated 48–100 h tests with pre- and post-operation characterization	Evaluate voltage evolution, reproducibility, and material stability

Table 10 Recommended experiments for extending and validating the findings of the present study.

5 Conclusions

This study provides an audited, evidence-weighted comparison of bare NF, NiFe-LDH/NF, and NiFe-LDH/Fe mesh in alkaline electrolyte with and without 0.33 M urea. Five conclusions follow directly from the acquired data.

1. **The nominal coating forms an open hierarchical morphology on both supports.** Representative SEM fields show micrometre-scale flower-like aggregates assembled from sheet-like features while preserving the open-cell NF and woven Fe-mesh architectures.
2. **NiFe-LDH/NF is the best-performing tested complete configuration.** It gave the lowest 90% iR-corrected E_{50} and E_{100} in both electrolytes: 1.471 and 1.499 V versus RHE in 1 M KOH, and 1.403 and 1.409 V in 1 M KOH + 0.33 M urea. Within the direct NF comparison, the coating improved moderate- and high-current polarization relative to bare NF.
3. **The benefit of urea is current-dependent rather than universal.** For NiFe-LDH/NF, urea lowered the matched-current potential by 68.2, 90.1, and 155.8 mV at 50, 100, and 500 mA cm^{-2}, respectively, but increased E_{10} by 26.6 mV. The low-current reversal is consistent with convolution by nickel oxidation/reconstruction. At moderate current, the response supports a strong UOR contribution; OER remains competing and product selectivity is unresolved.
4. **Tafel, EIS, and CV results are supporting descriptors, not stand-alone mechanistic proof.** Local apparent Tafel slopes fell after urea addition for all three configurations, yet the smallest slope did not correspond to the lowest absolute polarization. Coated NF showed a smaller fitted R_{ct} than bare NF within each electrolyte under the selected models, but the spectra were acquired at different and often drifting currents. Fifty CV cycles documented continuing electrochemical evolution rather than long-term durability.
5. **The stability record shows operability with measurable voltage drift.** NiFe-LDH/NF operated for 23.539 h at 100 mA cm^{-2} in urea-containing electrolyte. The mean corrected potential increased by 88.59 mV from the 0.5–1.0 h window to the final 0.5 h, while the final hour was comparatively narrow at 1.54799 ± 0.00171 V. A short fluctuation cluster near 16.6–16.7 h is consistent with bubble release.

Key finding

The actionable outcome is to advance NiFe-LDH/NF to replicated, product-resolved and full-cell testing. The current dataset establishes the strongest polarization performance among the tested configurations and a meaningful urea-dependent potential reduction at practical geometric current densities; the next experimental stage must determine whether that advantage corresponds to selective urea conversion, durable material integrity, and a lower measured hydrogen-production energy demand.

Acknowledgements

The author gratefully acknowledges Prof. Guanjie He for academic supervision and scientific direction, and Zekai Zheng for day-to-day laboratory mentorship, technical guidance, and constructive discussion of the electrochemical data. The author also thanks the Department of Chemistry at University College London for hosting the placement and providing access to laboratory and characterization facilities. The opportunity was enabled through the KAUST Academy Energy Specialization Summer Internship Program.

References

[1] Bryan K. Boggs, Rebecca L. King, and Gerardine G. Botte. Urea electrolysis: direct hydrogen production from urine. *Chemical Communications*, pages 4859–4861, 2009. doi: 10.1039/B905974A.

[2] Spencer W. Tatarchuk, Jason J. Medvedev, Feng Li, Yuliya Tobolovskaya, and Anna Klinkova. Nickel-catalyzed urea electrolysis: From nitrite and cyanate as major products to nitrogen evolution. *Angewandte Chemie International Edition*, 61:e202209839, 2022. doi: 10.1002/anie.202209839.

[3] Wei Ge, Lin Lin, Shi-Qiang Wang, Yi Wang, Xiaoming Ma, Qi An, and Liang Zhao. Electrocatalytic urea oxidation: advances in mechanistic insights, nanocatalyst design, and applications. *Journal of Materials Chemistry A*, 11:15100–15121, 2023. doi: 10.1039/D3TA02007J.

[4] Vignesh Vedharathinam and Gerardine G. Botte. Understanding the electro-catalytic oxidation mechanism of urea on nickel electrodes in alkaline medium. *Electrochimica Acta*, 81:292–300, 2012. doi: 10.1016/j.electacta.2012.07.007.

[5] Vignesh Vedharathinam and Gerardine G. Botte. Direct evidence of the mechanism for the electro-oxidation of urea on Ni(OH)2 catalyst in alkaline medium. *Electrochimica Acta*, 108:660–665, 2013. doi: 10.1016/j.electacta.2013.06.137.

[6] Xiaoxu Gao, Xue Bai, Peng Wang, Yao Jiao, Kieran Davey, Yao Zheng, and Shi-Zhang Qiao. Boosting urea electrooxidation on oxyanion-engineered nickel sites via inhibited water oxidation. *Nature Communications*, 14:5842, 2023. doi: 10.1038/s41467-023-41588-w.

[7] Hong Yang, Matthias Driess, and Prashanth W. Menezes. Self-supported electrocatalysts for practical water electrolysis. *Advanced Energy Materials*, 11:2102074, 2021. doi: 10.1002/aenm.202102074.

[8] Yanhua Diao, Yuan Liu, Guoxin Hu, Yujie Zhao, Yitong Qian, Hui Wang, Yuliang Shi, and Zhen Li. NiFe nanosheets as urea oxidation reaction electrocatalysts for urea removal and energy-saving hydrogen production. *Biosensors and Bioelectronics*, 211:114380, 2022. doi: 10.1016/j.bios.2022.114380.

[9] Hao Zhao, Yifan Zhang, Chen Xie, Jing Wang, Ting Zhou, Chen Zhou, Jia Li, Jin Bai, Xue Zhu, and Bin Zhou. Facile, controllable, and ultrathin NiFe-LDH in situ grown on a Ni foam by ultrasonic self-etching for highly efficient urine conversion. *Environmental Science & Technology*, 57:2939–2948, 2023. doi: 10.1021/acs.est.2c07282.

[10] Lena Trotochaud, Samantha L. Young, Jon K. Ranney, and Shannon W. Boettcher. Nickel–iron oxyhydroxide oxygen-evolution electrocatalysts: The role of intentional and incidental iron incorporation. *Journal of the American Chemical Society*, 136:6744–6753, 2014. doi: 10.1021/ja502379c.

[11] Daniel Friebel, Mary W. Louie, Michal Bajdich, et al. Identification of highly active Fe sites in (Ni,Fe)OOH for electrocatalytic water splitting. *Journal of the American Chemical Society*, 137:1305–1313, 2015. doi: 10.1021/ja511559d.

[12] Wei Zheng, Min Liu, and Leslie Y. S. Lee. Best practices in using foam-type electrodes for electrocatalytic performance benchmark. *ACS Energy Letters*, 5:3260–3264, 2020. doi: 10.1021/acsenergylett.0c01958.

[13] Alice Peugeot, Callum E. Creissen, Derya Karapinar, Hai N. Tran, Michael Schreiber, and Marc Fontecave. Benchmarking of oxygen evolution catalysts on porous nickel supports. *Joule*, 5:1281–1300, 2021. doi: 10.1016/j.joule.2021.03.022.

[14] Z. Li, G. Lin, L. Wang, et al. Seed-assisted formation of NiFe anode catalysts for anion exchange membrane water electrolysis at industrial-scale current density. *Nature Catalysis*, 7:944–952, 2024. doi: 10.1038/s41929-024-01209-1.

[15] O. van der Heijden, S. Park, J. J. J. Eggebeen, and M. T. M. Koper. Non-kinetic effects convolute activity and tafel analysis for the alkaline oxygen evolution reaction on NiFeOOH electrocatalysts. *Angewandte Chemie International Edition*, 62:e202216477, 2023. doi: 10.1002/anie.202216477.

[16] Tatsuya Shinagawa, Angel T. Garcia-Esparza, and Kazuhiro Takanabe. Insight on tafel slopes from a microkinetic analysis of aqueous electrocatalysis for energy conversion. *Scientific Reports*, 5:13801, 2015. doi: 10.1038/srep13801.

[17] Shuang Wang, Jianbo Zhang, Oumaima Gharbi, Vincent Vivier, Ming Gao, and Mark E. Orazem.

Electrochemical impedance spectroscopy. *Nature Reviews Methods Primers*, 1:41, 2021. doi: 10.1038/s43586-021-00039-w.

[18] Vincent Vivier and Mark E. Orazem. Impedance analysis of electrochemical systems. *Chemical Reviews*, 122:11131–11168, 2022. doi: 10.1021/acs.chemrev.1c00876.

[19] Andrea Angulo, Pieter van der Linde, Han Gardeniers, Miguel A. Modestino, and David Fernández Rivas. Influence of bubbles on the energy conversion efficiency of electrochemical reactors. *Joule*, 4:555–579, 2020. doi: 10.1016/j.joule.2020.01.005.

[20] Irfan A. Khan, Per Morgen, Raghunandan Sharma, and Shuang M. Andersen. Limitations of chronopotentiometry test protocols for stability study on oxygen evolution reaction electrocatalysts and recommendations. *The Journal of Physical Chemistry C*, 128:2828–2833, 2024. doi: 10.1021/acs.jpcc.3c07103.